

Article

Thiol-Based Probe Linker with Antifouling Properties for Aptasensor Development

Sandro Spagnolo¹, Katharina Davoudian², Soha Ahmadi², Edmund Chan², Tibor Hianik¹
and Michael Thompson^{2,*}

¹ Faculty of Mathematics, Physics and Informatics, Comenius University, Mlynská dolina F1, 842 48 Bratislava, Slovakia

² Department of Chemistry, University of Toronto, 80 St. George Street, Toronto, ON M5S 3H6, Canada

* Correspondence: m.thompson@utoronto.ca

Abstract: Surfaces with antifouling properties are critical for optimizing biosensors to improve the selectivity and specificity of analyte detection in complex biological samples. This work describes the four-step synthesis of 3-dithiothreitol propanoic acid (DTT_{COOH}), a new antifouling thiol linker that (a) significantly reduces fouling of raw human serum samples and (b) binds amino receptors via its terminal carboxylic acid group. DTT_{COOH} was successfully functionalized on quartz crystal microbalance (QCM) discs and used to anchor penicillin-binding aptamers. Relative to bare and coated (11-mercaptopundecanoic acid (MUA) and 1-undecanethiol (UDT)) QCM crystals, DTT_{COOH}'s antifouling improved by approximately 75–86%. Following aptamer/ethanolamine extension, the modified DTT_{COOH} layer reduced serum fouling by approximately 95–97% compared to bare and coated (MUA, UDT) crystals. QCM with dissipation (QCM-D) monitoring, contact goniometry, and cyclic voltammetry techniques were used to compare the DTT_{COOH} surfaces with quartz crystals functionalized with hydrophobic and hydrophilic molecules.

Keywords: antifouling linker; DNA aptamer; human serum; QCM-D; cyclic voltammetry; contact goniometry



Citation: Spagnolo, S.; Davoudian, K.; Ahmadi, S.; Chan, E.; Hianik, T.; Thompson, M. Thiol-Based Probe Linker with Antifouling Properties for Aptasensor Development. *Chemosensors* **2022**, *10*, 435. <https://doi.org/10.3390/chemosensors10100435>

Academic Editor: Chunsheng Wu

Received: 21 September 2022

Accepted: 17 October 2022

Published: 20 October 2022

Publisher's Note: MDPI stays neutral with regard to jurisdictional claims in published maps and institutional affiliations.



Copyright: © 2022 by the authors. Licensee MDPI, Basel, Switzerland. This article is an open access article distributed under the terms and conditions of the Creative Commons Attribution (CC BY) license (<https://creativecommons.org/licenses/by/4.0/>).

1. Introduction

Fouling or non-specific adsorption (NSA) of nontarget molecules limits biosensor applications significantly for detection in biological samples such as milk, whole blood, serum, or urine. In complex fluids, a variety of molecules, such as cells and proteins, can interfere with a biosensor's performance, reducing its sensitivity and specificity by fouling on the sensing surface [1]. Detecting analytes, particularly at low concentrations, requires antifouling properties to optimize a biosensor's sensitivity by increasing the signal-to-noise ratio [2]. Developing recognition surfaces on gold electrode biosensors with antifouling properties is an active area of research, particularly for optical, electrochemical, and piezoelectric biosensors.

Surface hydration can play a significant role in the antifouling properties of a biorecognition surface [3]. The structured interaction of interfacial water molecules on the sensing surface creates a "physical and energetic barrier" (Figure 1), preventing the adsorption of nontarget species [4–6]. If water molecules exist in a continuous interfacial hydration zone and work like a "water barrier," NSA is thermodynamically unfavorable [5].

Antifouling depends on the molecular properties of interfacial water molecules and the strength of the hydration layer on the sensing surface [4,5]. These properties include chain length, packing density, layer thickness, intermolecular interactions (such as hydrogen bonding and electrostatics), and/or functional groups of self-assembled monolayers (SAM). For example, a tightly packed, short-chain SAM can prevent NSA due to interfacial waters interacting with the recognition surface. While in addition to surface hydration, the

flexibility of long-chain SAMs can also influence antifouling, as compressing the layer induces steric repulsion, making fouling entropically unfavorable [3].

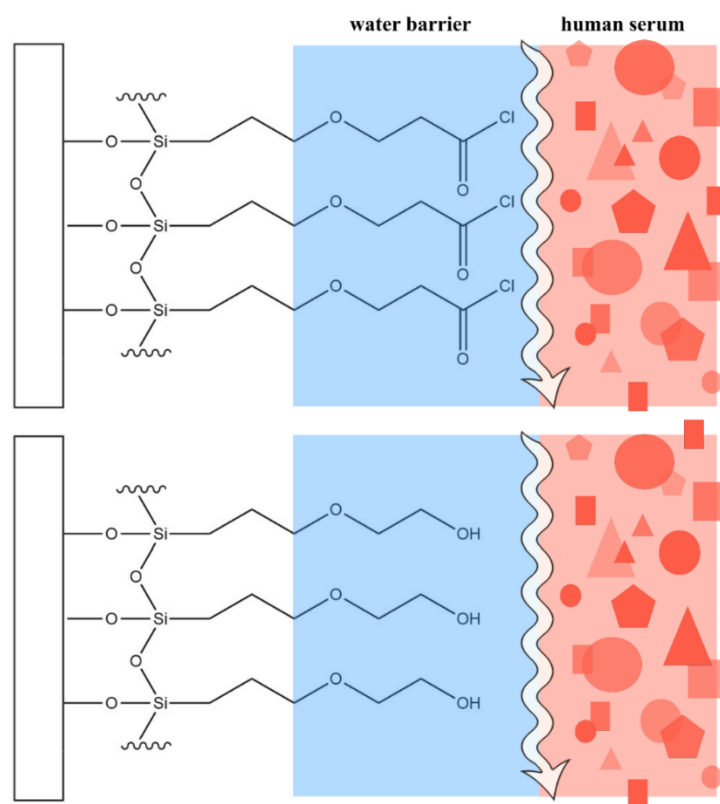


Figure 1. Hydrated MEG-Cl (above) and MEG-OH (below) adlayers on quartz with antifouling behavior.

We previously reported on the importance of surface hydration for the antifouling properties of organosilane-coated monoethylene glycol surfaces [5–7]. Poly- and oligoethylene glycol-based molecules represent a common class of antifouling agents, such as 2-(3-trichlorosilylpropoxy)-ethyl hydroxide (MEG-OH) and 3-(3-(trichlorosilyl)propoxy)propanoyl chloride (MEG-Cl). Our studies showed that the internal ether moiety is critical for forming the “water barrier,” allowing interfacial waters to penetrate and favorably interact with the self-assembled monolayer of the silane- [1,5,8] or sulfur-based linkers [7]. The effect of poly- and oligoethylene glycol derivatives on the antifouling properties of thiol-based linkers was also reported by other researchers [2,9].

MEG-Cl combines MEG-OH’s antifouling properties with linking functionality, as the acyl chloride can be modified with a biomolecular probe. Without linking MEG-Cl to a probe, a MEG-Cl coated surface experiences notably increased fouling in serum and milk, while a MEG-OH coating has negligible fouling. Most likely, the nucleophilic addition of water to MEG-Cl produces MEG-COOH, where the terminal carboxylic acid group becomes deprotonated in serum or milk [1]. We theorize that the negatively charged layer electrostatically interacts with positively charged species, making NSA more favorable relative to the neutral and hydrophilic MEG-OH surface.

The crystalline structure of quartz allows SAMs to functionalize less densely. A less dense layer can provide space for hydration between molecules to form the antifouling “water barrier.” Unlike quartz, functionalizing on gold surfaces can form a denser layer as compounds such as cysteine-containing proteins can covalently bind to gold via SH groups [7,10]. To facilitate a more effective “water barrier,” spacer molecules such as dithiols can be incorporated into the SAM.

Another challenge with using gold surfaces as sensing platforms is the significant NSA due to sulfur chemistry. Most thiol-based linkers have a carboxylic acid moiety that needs to be activated using 1-(3-(dimethylamino)propyl)-3-ethylcarbodiimide hydrochloride coupling with N-hydroxysuccinimide (NHS/EDC) allowing biomolecular probes to be covalently immobilized. However, some NHS-esters can remain unreacted with the probe, leading to the regeneration of the carboxylic acid group. The terminal carboxylic acid group can be deprotonated in fluids, such as serum or milk, causing the negatively charged layer to electrostatically interact with positively charged species, making NSA more favorable relative to the neutral and hydrophilic surface. Therefore, to prevent carboxylic acid regeneration, usually, a quenching reagent such as ethanolamine is used to react with unreacted NHS-esters [11]. While ethanolamine reacts with NHS-ester, it may also enhance the antifouling properties of the surface as its hydroxyl group can facilitate the “water barrier.”

To our knowledge, antifouling thiols on gold include poly- and oligoethylene glycol derivatives, zwitterions, and spacers such as dithiothreitol (DTT). Chávez et al. tested O-(2-Mercaptoethyl)-O'-methyl-hexa(ethylene glycol) SAMs, where the chains were made up of seven ethylene glycol units (EG7); the EG7 layer demonstrated a significant decrease in fouling [9]. Bertok et al. designed a mixed zwitterionic antifouling layer with carboxybetaine and sulfobetaine, which allow interfacial molecules to also bind electrostatically [12]. Wu et al. described a ternary monolayer system involving DTT, a thiolated oligonucleotide probe (SHCP), and 6-mercapto-1-hexanol (MCH). Compared to the binary SHCP + MCH layer, the introduction of DTT provided a more compact SAM and polar functional groups that increased the signal-to-noise ratio. While DTT's hydroxyl groups support an antifouling “water barrier,” the sensor was not tested in undiluted raw serum or urine [13].

This study presents a novel thiol molecule, 3-dithiothreitol propanoic acid (DTT_{COOH}), that can be used as a linker for developing biorecognition surfaces of biosensors with excellent antifouling properties (Figure 2). DTT_{COOH} is a derivative of DTT, where one hydroxyl group is modified to propanoic acid to allow for probe immobilization by NHS/EDC. We hypothesize that DTT_{COOH} facilitates the creation of a “water barrier” as the dithiol structure induces a more effective hydration network by providing distance between the propanoic acid chains of the SAM, increasing the surface area for the interfacial water molecules. In addition to its antifouling and linking properties, DTT_{COOH} involves a straightforward and cost-effective four-reaction synthesis. The synthesis can be reduced to three reactions with the purchase of oxidized dithiothreitol (Ox-DTT).

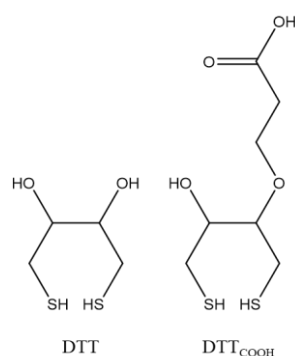


Figure 2. Dithiothreitol (DTT) and 3-dithiothreitol propanoic acid (DTT_{COOH}).

DTT_{COOH}'s antifouling capability against untreated human serum was assessed using the quartz crystal microbalance with dissipation monitoring (QCM-D). QCM-D is a mass-sensitive sensor involving layers immobilized on the gold surface of a piezoelectric quartz disc. An applied electric field oscillates the disc, allowing changes in mass on the disc's surface to be detected by a frequency shift relative to the crystal's fundamental resonance

(Δf) [14]. A layer's viscoelasticity can be measured by changes in dissipation (ΔD), which assesses total energy losses through a layer's deformation. The more flexible the layer, the greater the deformation and the higher the dissipation shift [15–17].

Human serum fouling was quantified using QCM-D, allowing for DTT_{COOH}'s antifouling to be compared to other thiol layers (11-mercaptoundecanoic acid (MUA), 1-undecanethiol (UDT), and DTT) and bare QCM crystals. We examined the antifouling properties of a QCM-based aptasensor using DTT_{COOH} as a linker to immobilize aptamers. The functionalized layers of the crystals were confirmed and compared using contact angle goniometry (CAG) and cyclic voltammetry (CV).

2. Materials and Methods

2.1. Materials

Sodium iodide, sodium chloride, sodium carbonate, sodium thiosulfate, anhydrous magnesium sulfate, and absolute ethanol were analytical grade and obtained from Sigma-Aldrich (St. Louis, Mo, USA). All other organic solvents (acetonitrile, dichloromethane, ethyl acetate, hexane, methanol) were ACS grade or better and supplied by Sigma-Aldrich (St. Louis, Mo, USA). N-Benzyltrimethylammonium hydroxide (40% in methanol *w/w*) and ammonium hydroxide (28–30% in water *w/v*) were supplied by Fisher Scientific (Ottawa, ON, Canada). Hydrogen peroxide (30% in water *w/w*), T-butyl acrylate, trifluoroacetic acid, zinc, 1-undecanethiol, 11-mercaptoundecanoic acid, dithiothreitol, β -mercaptoethanol, NHS, EDC, and ethanolamine were supplied by Sigma-Aldrich (St. Louis, Mo, USA) and used without further purification. All aqueous solutions were prepared with Milli-Q water (18.20 M Ω cm).

The lyophilized aptamers (5'NH₂-TCC CTA CGG CGC TAA CCT CCC AAC CGC TCC ACC CTG CCT CCG CCT CGC CAC CGT GCT ACA AC-3' against *Staphylococcus aureus* and 5'NH₂-CTG AAT TGG ATC TCT CTT CTT GAG CGA TCT CCA CA-3' against penicillin) were purchased from Generi Biotech (Hradec Králové, Czech Republic). Penicillin was purchased from Sigma-Aldrich (St. Louis, Mo, USA). Phosphate-buffered saline (PBS) was prepared with 137 mM NaCl, 2.7 mM KCl, 10 mM Na₂HPO₄, and 1.8 mM KH₂PO₄ at pH 7.4 and filtered with a 0.22 μ m membrane filter (Merck-Millipore, Darmstadt, Germany). Human serum was collected from a healthy donor. Incorporating human blood in this work took place in full compliance with the ethical rules on the use of human tissues for experimentation and research. The healthy donor voluntarily donated blood and was informed about its use. Furthermore, the donor remained anonymous and no genetic or metabolic information from the biological sample was collected.

2.2. Synthesis of 3-Dithiothreitol Propanoic Acid (DTT_{COOH}) Linker

Sodium iodide (3.24 mg, 21.6 μ mol, 0.01 equiv.) was added to a stirred solution of dithiothreitol (343.8 mg, 2.22 mmol) in ethyl acetate (18 mL) at room temperature. Hydrogen peroxide was then added dropwise (30% aqueous solution, 0.5 mL, 4.89 mmol). The reaction was stirred for 85 min at room temperature (approximately 23 °C), during which the solution changed from colorless to orange-brown, characteristic of the generated iodine. The reaction mixture was then quenched with saturated aqueous sodium thiosulfate and the organic layer was further washed with saturated aqueous sodium carbonate (12 mL) followed by saturated aqueous sodium chloride (12 mL). The organic phase was then dried over anhydrous magnesium sulfate and filtered. The volatiles were evaporated under reduced pressure to yield oxidized DTT (Ox-DTT) as a white powder (330 mg, 97.5% yield in mol) (Figure 3). ¹H and ¹³C NMR spectra confirmed the purification of the product (Figures S1 and S2 of Supplementary Material).

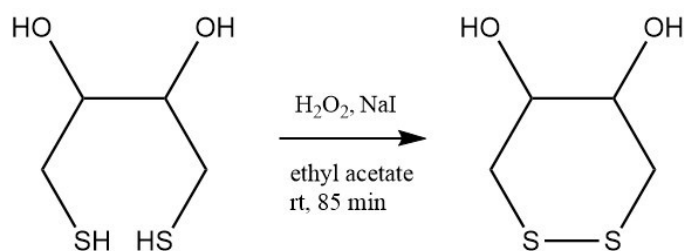


Figure 3. Oxidation of dithiothreitol.

In an oven-dried flask, N-Benzyltrimethylammonium hydroxide (40% *w/w* in methanol, 300 μL , 276 mg, 1.65 mmol) was concentrated under vacuum and cooled to room temperature. Ox-DTT (100 mg, 0.65 mmol) in acetonitrile (10 mL) was added to this solution. The reaction mixture was stirred at room temperature for 15–30 min under an inert atmosphere. Tert-butyl acrylate (143.5 μL , 1.00 mmol) was added and the mixture was stirred at 58–60 $^{\circ}\text{C}$ for 72 h. The residue was filtered through a silica plug to remove the colored impurities, then subjected to flash chromatography (3:1 *v/v* hexane/ethyl acetate) using high-grade silica gel (60 \AA pore size, 200–400 mesh) which produced tert-butyl 3-(DTT)propanoate (TBu-Ox-DTT) with a 55.7% yield (102.7 mg, 0.37 mmol) (Figure 4). ^{13}C NMR spectra confirmed the purification of the product of this reaction (Figure S3 of Supplementary Material).

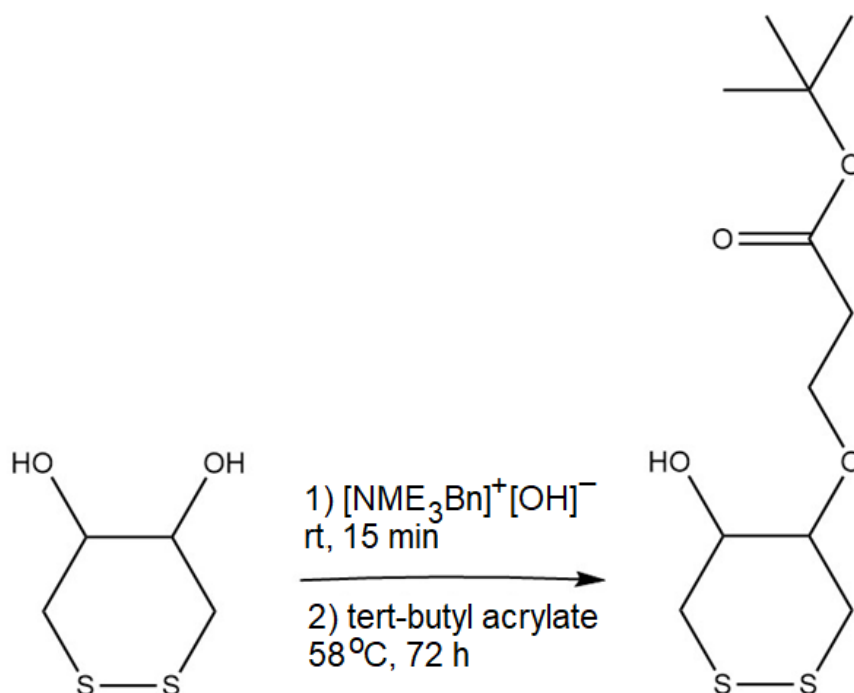


Figure 4. Conversion of oxidized DTT to tert-butyl 3-(DTT)propanoate.

During the reaction, the product was monitored with thin layer chromatography using 3:1 *v/v* hexane/ethyl acetate eluent (Figure 5). The reaction was stopped at the appearance of the hydrophobic products (C spots) which may contain the compound with both hydroxyl groups modified to tert-butyl propanoate. The C spots were removed with the subsequent flash chromatography and the desired product, TBu-Ox-DTT (B spot), was purified. Ox-DTT (A spot) was also saved for repeating the reactions.

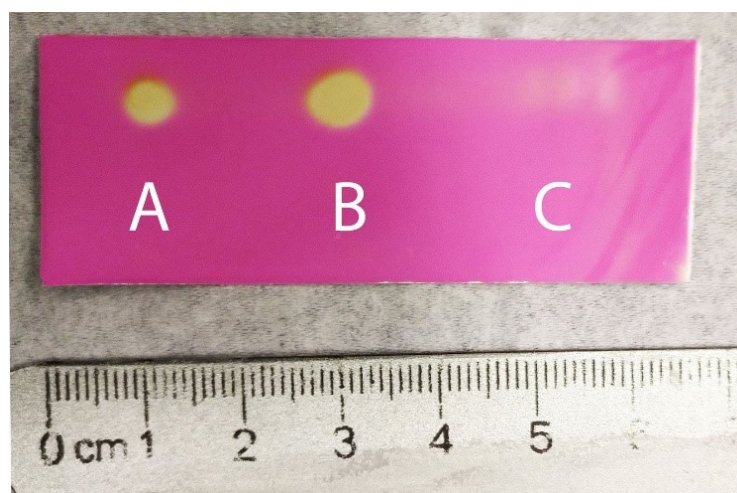


Figure 5. Thin-layer chromatography showing (A) ox-DTT, (B) tert-butyl 3-(DTT)propanoate, and (C) hydrophobic products.

TBu-Ox-DTT (27.7 mg, 99.28 μmol) and trifluoroacetic acid (46 μL , 6 equiv.) were dissolved in dichloromethane (2 mL). The mixture was stirred at room temperature for 60–90 min. The volatiles were concentrated under vacuum. To ensure the complete removal of trifluoroacetic acid, the residue was repeatedly diluted with additional dichloromethane and evaporated under reduced pressure to yield 80.8% 3-(DTT)propanoic acid (Ox-DTT_{COOH}) (18 mg, 80.21 μmol).

Ox-DTT_{COOH} (26.3 mg, 117.25 μmol) was dissolved in a solution of 1% trifluoroacetic acid in acetonitrile (10 mL). Powdered zinc (200 mg, 3 mmol) was added, and the solution was stirred for 2 h at room temperature. The reaction was centrifuged at 7500 RPM for 10 min. The supernatant was decanted and concentrated under reduced pressure. The residue was repeatedly diluted with dichloromethane, which was then evaporated under vacuum, yielding 85.1% 3-(DTT)propanoic acid (DTT_{COOH}) (22.39 mg, 99.78 μmol) (Figure 6). ¹H and ¹³C NMR spectra confirmed the purification of the final product (Figures S7 and S8 of Supplementary Material).

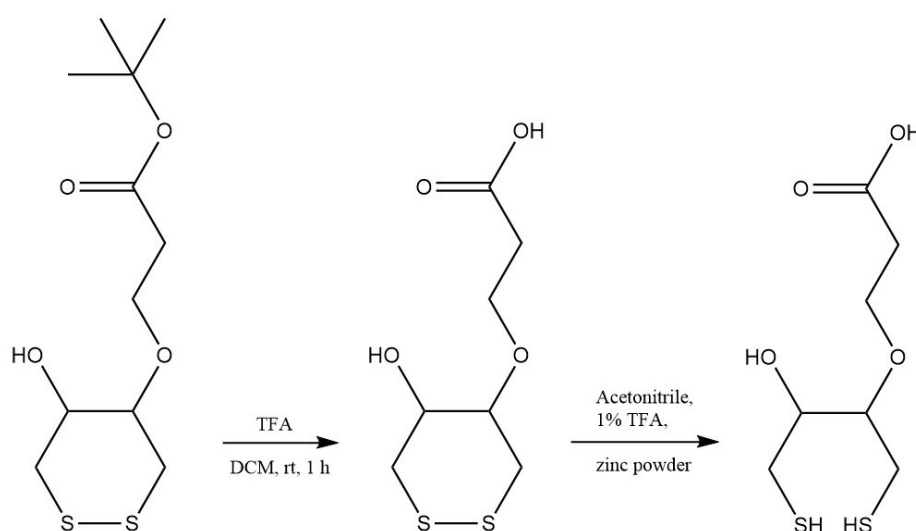


Figure 6. Deprotection and reduction reaction steps to produce DTT_{COOH}.

All the reagents used for the synthesis of DTT_{COOH} were handled in the fume hood, as they are irritating to the eyes and respiratory tract (sodium iodide, hydrogen peroxide, ethyl acetate, and n-hexane), toxic if swallowed or inhaled and in contact with skin (N-

benzyltrimethylammonium hydroxide, trifluoroacetic acid, DCM, and acetonitrile), and harmful by ingestion, inhalation, and skin absorption (tert-butyl acrylate).

2.3. Aptamer Stock Solution Preparation

The aptamers were chosen according to availability. The lyophilized aptamers were resuspended in 10 mM Tris and 1 mM EDTA buffer at pH 8.0 in DNase-free Milli-Q water to prepare a 100 μ M stock solution. Afterward, the solution was diluted into 10 μ M aliquots (100 μ L) with PBS. The aptamer aliquots were stored at -20 $^{\circ}$ C and thawed individually prior to each experiment.

2.4. Cleaning and Surface Modification of QCM Crystals

Quartz crystals (AT-cut with gold electrodes on both sides, 0.2 cm² sensing area, 8 MHz fundamental resonant frequency) were purchased from Total Frequency Control Ltd., Storrington, UK. Each crystal was cleaned in three 25 min cycles of basic Piranha solution (7 mL of 1:1:5 *v/v/v* of 28–30% NH₄OH, 30% H₂O₂, and Milli-Q water) at 70 $^{\circ}$ C. The crystals were washed with copious amounts of Milli-Q water ($\times 3$) in between cycles. Following the third cleaning, the crystals were rinsed with Milli-Q water ($\times 2$) and methanol ($\times 2$).

The clean quartz crystals were individually functionalized on an orbital shaker by soaking in 2 mL solutions of 2 mM UDT, 2 mM MUA, 50 μ M DTT, or 50 μ M DTT_{COOH} in absolute ethanol overnight. The DTT_{COOH} crystals were further functionalized with 2 mL solutions in the following order: 1 mM β -mercaptoethanol in absolute ethanol for 10 min, NHS/EDC (20 mM NHS and 50 mM EDC) in Milli-Q water for 35 min, 5 μ M of aptamer in Milli-Q water for 70 min, and 1 M ethanolamine in Milli-Q water for 40 min. For preparing NHS/EDC, 0.8 mL NHS and 1.2 mL EDC aliquots were made separately and combined before functionalization. In between changing solutions, each crystal was washed with Milli-Q water ($\times 2$). Alternatively, the crystals were functionalized with DTT_{COOH} in-flow (Figure 7).

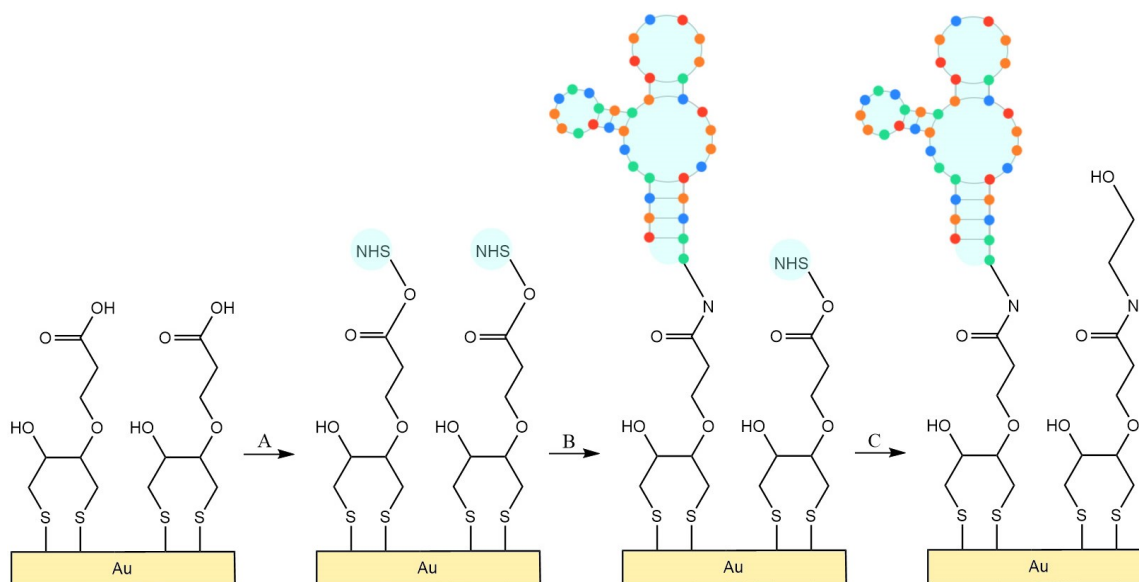


Figure 7. Surface modification of QCM crystals. Following DTT_{COOH}, the crystals were functionalized with β -mercaptoethanol (not shown), then (A) NHS/EDC, (B) aptamer, and (C) ethanolamine.

Before measurements, the SAM-functionalized crystals were gently dried under a flow of nitrogen.

2.5. Contact Angle Goniometry (CAG)

The KSV CAM 101 contact angle goniometer (KSV Instruments Ltd., Helsinki, Finland) was used for static contact angle goniometry (CAG) with Milli-Q water under ambient conditions. The results were elaborated by the instrument's software. Bare and coated QCM crystals were measured on the gold electrode surface to confirm functionalization. A minimum of three readings with different crystals were recorded and averaged.

2.6. QCM Set-Up and Measurements

The bare and modified crystals were prepared, mounted, and secured using O-rings in an acryl flow-through cell (JKU, Linz, Austria). A holder clamped the cell to keep the internal gold laminar conductors in contact with the crystal's gold electrodes, which also secured the connection to a SARK-110 vector analyzer (Seed, Shenzhen, China). The analyzer was connected to a controller via universal serial bus (USB) for setting the parameters and collecting data by a Python software [18].

One crystal face was exposed to the cell chamber, where liquid flowed through inside. A GeniePlus syringe pump (Kent Scientific, Torrington, CT, USA) and a pulling syringe drew the solutions from a vial into the cell chamber by an inlet pipe, which then flowed away through an outlet pipe to the syringe.

The experiments were performed at fundamental frequency, 8 MHz, in a constant flow of $50 \mu\text{L min}^{-1}$, at room temperature (approximately 23°C). Untreated human serum was used as a fouling agent while the remaining solutions functionalized the DTT_{COOH} crystals for building the aptasensor. In flow mode, the QCM crystal was initially washed with PBS buffer to remove any weakly adsorbed thiols on the gold surface and to obtain a stable baseline (about 55–60 min). Subsequently, the flow was switched with human serum samples and bare, UDT, MUA, DTT, and DTT_{COOH} crystals were incubated for 5 min.

For the aptasensor, after the DTT_{COOH} crystals reached an initial baseline, different concentrations were flowed into the chamber. Initially, a solution containing NHS/EDC was flowed for 35 min, during which the linker's carboxyl groups were activated. Then a PBS wash for 5 min was performed. Subsequently, the surfaces were incubated with the aptamer solution for 90 min, and a PBS wash followed. The crystals were then incubated with an ethanolamine solution to neutralize the remaining activated carboxyl groups of the linker. After these surface modifications, the SAM should lose the negative charges that contribute to serum fouling. After another 5 min of PBS wash, the surfaces were finally incubated with β -mercaptoethanol for 10 min to potentially passivate any part of the surface without a linker. A final PBS wash for 15 min rinsed the crystal to remove weakly adsorbed compounds and improve the signal's stabilization for the next step, the antifouling test.

After the aptasensor was built, it was tested with a 5 min incubation with human serum to evaluate its antifouling properties. The crystals were then rinsed with PBS buffer to remove the sample from the chamber and obtain a stable baseline.

2.7. QCM Data Analysis

The antifouling measurements were performed for a minimum of three times to record raw data that were fitted by a Python script. The script uses an equation from Yoon et al.'s paper [19] to calculate the peak parameters. The fitted data were then plotted with Excel and statistically processed as mean \pm standard deviation (SD).

The aptasensor's antifouling properties were evaluated in triplicate by functionalizing in-flow with multiple steps. The aptasensor's ability to bind the analyte (penicillin) was also evaluated.

More measurements with different penicillin concentrations were not performed as the aim of this work was the synthesis and characterization of the new dithiol, DTT_{COOH} , for reducing the fouling from raw samples and its application in sensor technology.

2.8. Electrochemical Measurements

All electrochemical experiments were carried out using a CHI440A potentiostat (CH Instruments, Austin, TX, USA) with a three-electrode setup: a disposal gold electrode (0.2 cm²), Pt wire, and Ag/AgCl as the working electrode, the auxiliary electrode, and the reference electrode, respectively. The Ag/AgCl reference electrode was connected to an electrochemical cell through a salt bridge, filled with agar and 1 M KNO₃, to minimize the diffusion of chloride ions into the electrolyte solution. Experiments were performed by immersing the electrodes and salt bridge in 25 mL aqueous solutions of 5 mM K₄[Fe(CN)₆]/K₃[Fe(CN)₆] as a redox probe containing 0.5 M KCl as a supporting electrolyte. Cyclic voltammetry (CV) and square wave voltammetry (SWV) were employed to monitor the current response as a function of applied potential. CV measurements were started at the open circuit potential (OCP) with positive initial scan polarity and 5 sec quiet. The scan rate of 0.1 V/s was applied unless otherwise mentioned. The SWV experiment was performed with an amplitude of 2.5 mV, a frequency of 15 Hz, and a 2 sec quiet time. The conventional SWV experiments were followed by the reverse scan to monitor both oxidation and reduction reactions. This approach provides data that are equivalent to cyclic square wave voltammetry (CSWV) [20]. The gold electrodes were modified in the same way as the QCM crystals.

3. Results and Discussion

3.1. Contact Angle Goniometry Analysis

The different SAM functionalization of the gold electrode surfaces were confirmed with CAG (Figure 8). The surface angle on bare gold after piranha treatment was approximately 56° ± 4°, which is similar to 49°–65° reported in the literature for bare gold [21–23]. Contact angle measurements of UDT-modified surfaces had an average of 105° ± 2°, which is significantly higher compared to bare gold and indicates that the surface was successfully functionalized with the hydrophobic UDT layer. This result is comparable to values present in the literature for hydrophobic surfaces [24,25]. For MUA-modified surfaces, the contact angle was about 48° ± 14°, which is lower than bare and UDT crystals due to MUA's hydrophilicity given by its carboxyl group [23,26].

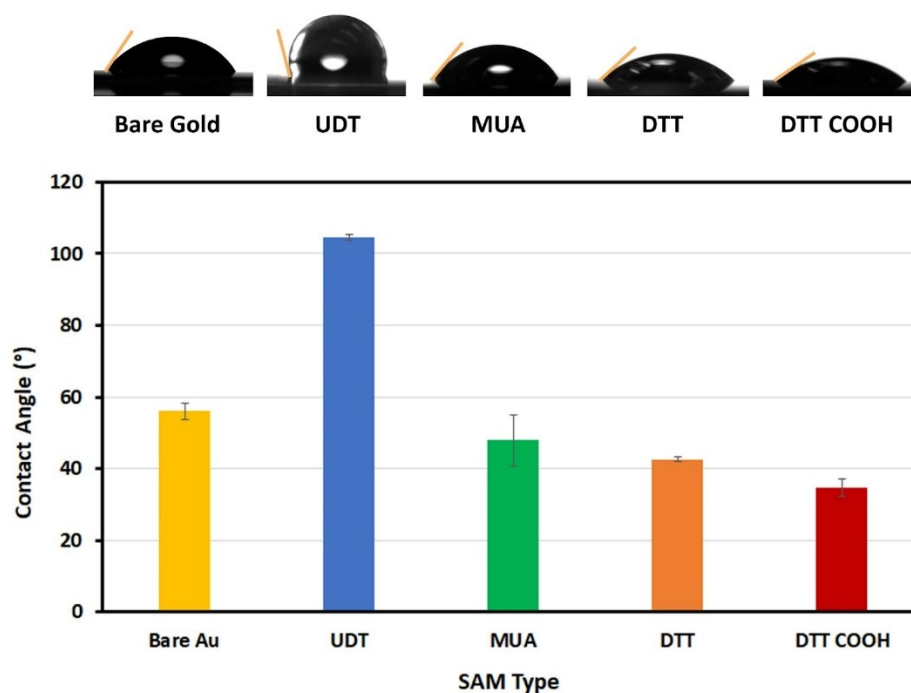


Figure 8. Contact angles of Milli-Q water droplets on gold electrodes with different SAM coatings.

DTT- and DTT_{COOH}-modified QCM crystals had angles of $43^\circ \pm 1^\circ$ and $35^\circ \pm 5^\circ$, respectively. DTT's contact angle has a similar trend to values in the literature [27,28]. These results confirmed surface modification, as DTT and DTT_{COOH} SAMs were more hydrophilic compared to bare gold.

While CAG is useful for confirming functionalization, it does not indicate the SAM's density. We expect a disordered DTT_{COOH} layer as DTT binding to gold has been confirmed to be in a disordered way. As a less dense SAM is more likely to have vacancy islands due to gold surface atoms rearranging during thiol functionalization [27], in this work, we used β -mercaptoethanol to passivate any exposed gold which could be easily subject to NSA. To estimate the density of DTT_{COOH}'s SAM, incubating QCM discs in-flow with DTT_{COOH} followed by a linear thiol molecule is an object of further investigation.

3.2. Electrochemical Characterization of the Aptasensor

Electrochemical experiments were performed to further investigate the surface properties of the aptasensor. We applied cyclic voltammetry (CV) and square wave voltammetry (SWV) to characterize each step of surface modification of the gold electrodes using 5 mM $K_4[Fe(CN)_6]/K_3[Fe(CN)_6]$ as an external redox probe. Figure 9 shows the conventional SWV experiments followed by the reverse scan to monitor both oxidation and reduction reactions; this approach provides data that are equivalent to cyclic square wave voltammetry (CSWV) [20]. The decline in SWV current intensity after DTT_{COOH} modification is due to producing a self-assembled monolayer of DTT_{COOH} on the gold electrodes, which also results in increasing the peak-to-peak separation of the redox signals in the CV (see Figure S6 of Supplementary Material). Although the current intensity was expected to decrease significantly after the final modification step, the current intensity increased (Figures 9 and S6), indicating that the aptamer may be involved in electron transfer.

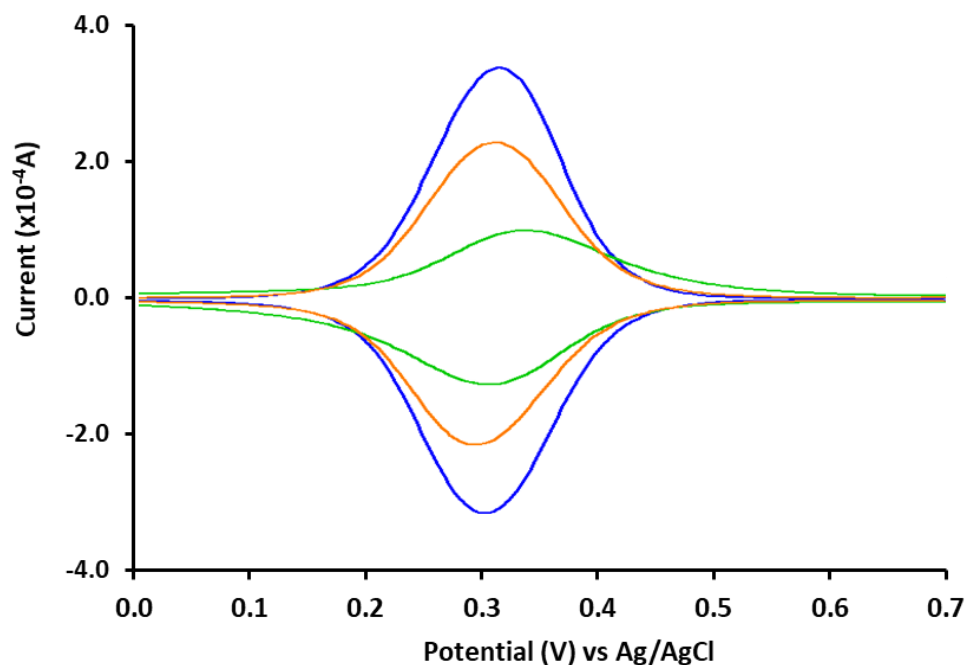


Figure 9. Square wave voltammogram (SWV): oxidation and reduction signals of the gold electrode (blue), after modification with DTT_{COOH} (green), and after modification with aptamer (orange). All experiments were carried out using a three-electrode setup with a gold electrode, a Pt wire, and Ag/AgCl electrode as the working electrode, the auxiliary electrode, and the reference electrode, respectively, in 5 mM $[Fe(CN)_6]^{3-/4-}$ as the redox probe containing 0.5 M KCl as the supporting electrolyte. The SWV experiments were performed with an amplitude of 2.5 mV, a frequency of 15 Hz, and a 2 sec quit time.

The unexpected electrochemical activity of aptamers was already reported by Alawad et al. [29]. They showed that immobilization of a 76-mer aptamer on a modified electrode reduced the electron transfer resistance of the Faradaic impedance spectra. Their investigation confirmed that the aptamer is intrinsically electroactive and can be used as a recognition element. Aptamer electroactivity can be due to the redox activity of its purines and pyrimidines. The redox reaction of nucleic acids was observed in solution as well as on different surfaces, such as glassy carbon, graphene-based, nanocarbon-based, boron-doped diamond, and gold electrodes [30–32]. It should be noted that aptamers have an overall negative charge, which may have two different effects when immobilized on the electrode surface. (1) It can provoke electrostatic repulsion between the electrode surface and the negatively charged $[\text{Fe}(\text{CN})_6]^{3-}/[\text{Fe}(\text{CN})_6]^{4-}$ redox couple in the solution leading to a decrease in the rate of electron transfer and thus a decrease in the current intensity, or (2) it can provoke electrostatic repulsion of neighboring aptamers, forcing the aptamers into a relatively linear conformation, thereby rendering the aptamer film on the electrode permeable to the electron transfer leading to an increase in current intensity [33].

A study by Tan et al. [34] showed that a high concentration of K^+ can neutralize all the electronegative sites of the aptamer. Therefore, as our electrochemical experiments were performed in the presence of high K^+ concentration, we can hypothesize that a positively charged shelter is created around the aptamer leading to an overall positive charge of the electrode surface. This leads to physisorption of the negatively charged $[\text{Fe}(\text{CN})_6]^{3-}/[\text{Fe}(\text{CN})_6]^{4-}$ redox couple on the electrode surface causing an increase in the rate of electron transfer and thus an increase in current intensity.

Therefore, an increase in current intensity after immobilization of aptamer can be due to (1) the electrostatic repulsion of neighboring aptamers causing a more permeable biofilm on the electrode or (2) physisorption of $[\text{Fe}(\text{CN})_6]^{3-}/[\text{Fe}(\text{CN})_6]^{4-}$ redox couple on the file as the result of high K^+ concentration. To examine these two hypotheses, we performed a CV experiment at different scan rates (Figure 10) to study the electron transfer process. The electron transfer process can be diffusion-controlled, which relates to the redox activity of electroactive species, $[\text{Fe}(\text{CN})_6]^{3-}/[\text{Fe}(\text{CN})_6]^{4-}$, in solution near the surface, or it can be adsorption-controlled, which relates to redox activity or the ability of electron transfer of the active sites on the surface. The first hypothesis correlates with a diffusion-controlled electron transfer process while the second hypothesis correlates with an adsorption-controlled electron transfer process.

The diffusion-controlled redox process can be described mathematically by the Randles-Sevcik equation:

$$I_p = 2.68 \times 10^5 n^{3/2} A D^{1/2} c v^{1/2}$$

where I_p , n , D , A , c , and v are peak current, number of electrons, diffusion coefficient, electrode area, concentration, and the scan rate, respectively. Therefore, a linear relationship between the current and square root of the scan rate indicates that the redox process is diffusion-controlled while a linear relationship between the current and scan rate indicates that the redox process is adsorption-controlled. While plotting current intensity (oxidation/reduction peaks) for modified gold electrodes after incubation in DTT_{COOH} showed a linear relationship with the square root of scan rates ($R^2 > 0.99$) (Figure S7 of Supplementary Material), the plot of the current intensity of the aptasensor did not have a linear relationship with either square root of scan rates or scan rates (Figure 10D and Figure S8 of Supplementary Material). These results confirmed that the DTT_{COOH} modification did not affect the diffusion-controlled electron transfer process of $[\text{Fe}(\text{CN})_6]^{3-}/[\text{Fe}(\text{CN})_6]^{4-}$ on the gold electrode, while aptamer modification affected the electron transfer process. However, at scan rates below 0.4 V/s the current intensity (both oxidation and reduction signals) of the aptasensor has a linear relationship with the square root of scan rates ($R^2 > 0.99$) but not with the scan rate ($R^2 < 0.96$), indicating that at low scan rate the electron transfer is a diffusion-controlled process with fast kinetics. In other words, at a low scan rate, the diffusion-controlled process is dominant, which confirms the

first hypothesis, while at higher scan rates the adsorption-controlled process may also be involved in electron transfer, which shows the possibility of the second hypothesis.

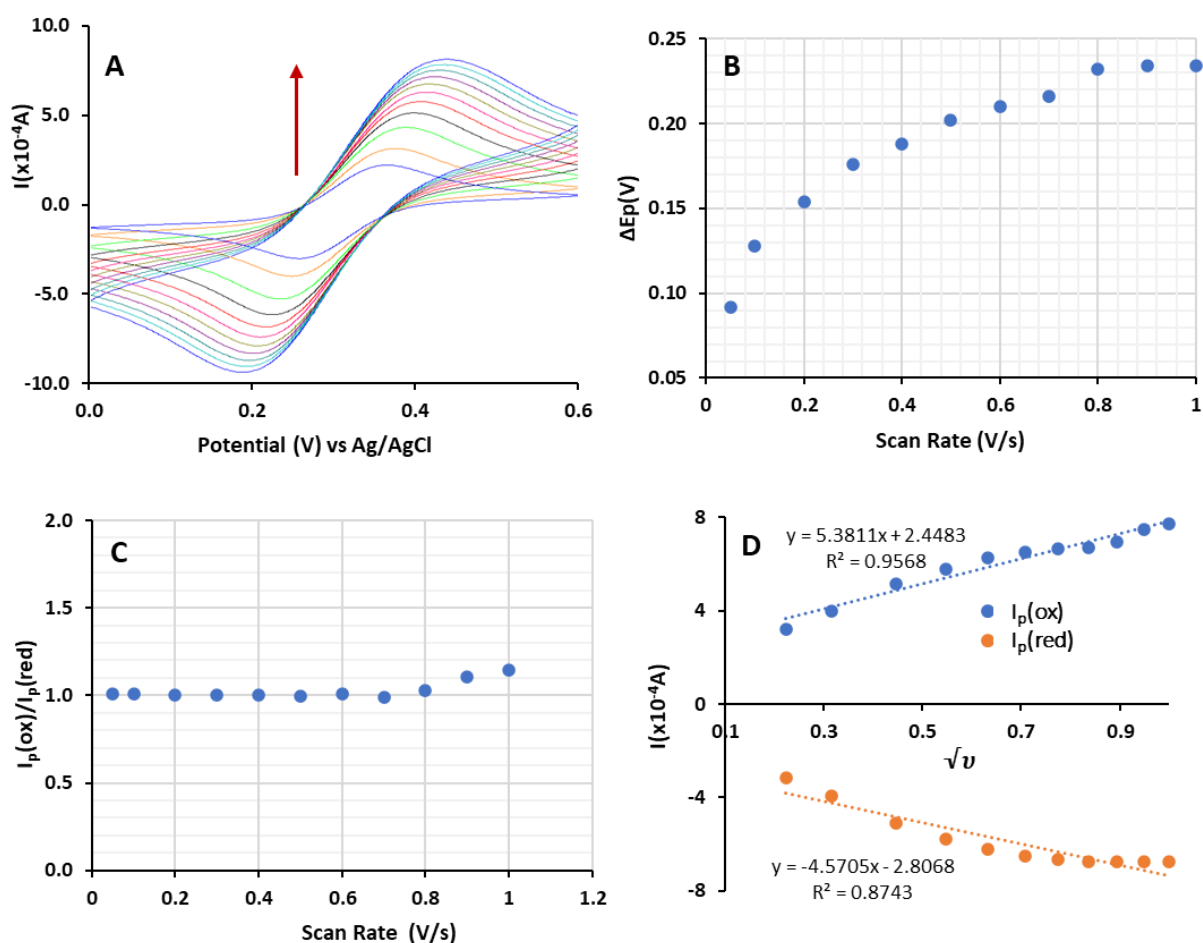


Figure 10. The influence of scan rate on the electrochemical response (CV) of the aptasensor using 5 mM $[\text{Fe}(\text{CN})_6]^{3-/4-}$ as a redox probe containing 0.5 M KCl as a supporting electrolyte. All experiments were carried out using a three-electrode setup with a gold electrode, a Pt wire, and Ag/AgCl electrode as the working electrode, the auxiliary electrode, and the reference electrode, respectively. CV experiments started at the open circuit potential (OCP) with positive initial scan polarity, sample interval of 2 mV, and with varying scan rate from 0.05 V/s to 1.0 V/s. (A) Cyclic voltammograms. Red arrow shows increase in the scan rate, (B) Graph of the peak potential separation ($\Delta E_p = E_p(\text{ox}) - E_p(\text{red})$) vs. scan rate, (C) Graph of $I_p(\text{ox})/I_p(\text{red})$ vs. scan rate, (D) Graph of current vs. square root of scan rate for $I_p(\text{ox})$ (blue curve) and $I_p(\text{red})$ (orange curve).

The reversibility of the redox reaction of $[\text{Fe}(\text{CN})_6]^{3-}/[\text{Fe}(\text{CN})_6]^{4-}$ can also be examined by CV at different scan rates. Our results indicate that by increasing the scan rate, the $I(\text{ox})/I(\text{red})$ increases to 1.1 and the peak potential separation is increased indicating that the rate of oxidation is higher than reduction and the redox reaction is irreversible (see Figure 10B,C). We can conclude that at a lower scan rate the observed current is mostly due to the redox reaction of $[\text{Fe}(\text{CN})_6]^{3-}/[\text{Fe}(\text{CN})_6]^{4-}$ in solution close to the surface, but at higher scan rate, both diffusion and adsorption may be involved in the electron transfer process causing lower reduction rate. As we mentioned earlier, the diffusion-controlled process could be due to the formation of a relatively linear conformation of the aptamer, which enhances the permeability of the self-assembled monolayer on the gold electrode. The adsorption-controlled process could be due to the formation of a positively charged shield around the aptamer layer that adsorbs the $[\text{Fe}(\text{CN})_6]^{3-}/[\text{Fe}(\text{CN})_6]^{4-}$ redox couple on the

electrode surface. The electroactivity of the aptamer can also contribute to electron transfer through the adsorption-controlled process. Further investigation is needed to determine the relative contribution of these processes in the electron transfer of the aptasensor.

3.3. Serum Antifouling Test with Quartz Crystal Microbalance

With QCM-D, the frequency and dissipation variations were quantified to measure adsorbed human serum material (Figure 11). As human serum adsorbs to hydrophobic surfaces, non-antifouling layers of MUA and UDT were used to compare and determine DTT_{COOH}'s antifouling. MUA was chosen as it is typically a linker on gold electrode surfaces due to its thiol and carboxylic acid groups.

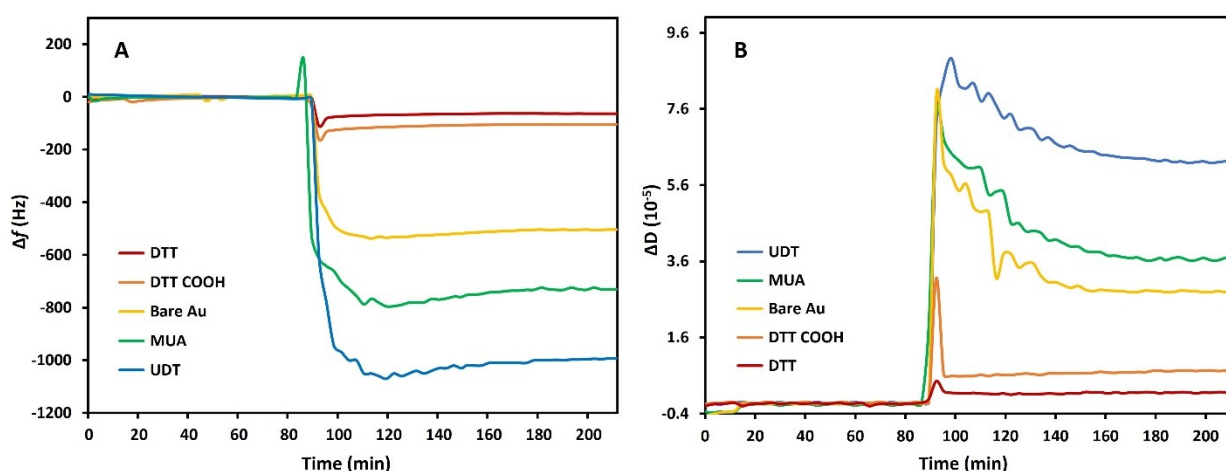


Figure 11. The (A) frequency and (B) dissipation shifts on gold electrodes with different SAM coatings following exposure to undiluted human serum.

Based on the data in Table 1, MUA's aliphatic structure and carboxyl group induced significant resonant frequency (653 ± 50 Hz) and dissipation variations ($3.6 \pm 0.5 \times 10^{-5}$) caused by serum fouling, while UDT's sole aliphatic structure caused the highest shifts in the frequency (900 ± 141 Hz) and dissipation ($6.5 \pm 0.1 \times 10^{-5}$) following adsorption of serum material due to increased hydrophobicity. The frequency and dissipation shifts are increased for hydrophobic surfaces, as more bioorganic matter is adsorbed.

Table 1. Frequency and dissipation shift after exposure to undiluted human serum and subsequent wash with PBS.

SAM	Avg. $\Delta f \pm$ St. Dv. MILOS (Hz)	% Fouling Relative to MILOSDTT _{COOH}	Avg. $\Delta D \pm$ St. Dv. MILOS (10^{-5})
Bare Au	501.7 ± 28.9	75	3.1 ± 0.2
UDT	900.4 ± 141.4	86	6.5 ± 0.1
MUA	653.3 ± 50.3	81	3.6 ± 0.5
DTT _{COOH}	126.9 ± 33.9	-	0.9 ± 0.2
DTT	99.7 ± 42.4	-21	0.5 ± 0.3

Measurements of bare crystals demonstrated a frequency shift of 502 ± 29 Hz and dissipation shift of $3.1 \pm 0.2 \times 10^{-5}$ following human serum incubation, while serum adsorption on DTT_{COOH} surfaces caused the frequency (127 ± 34 Hz) and dissipation ($0.9 \pm 0.2 \times 10^{-5}$) to shift less than uncoated and coated (UDT and MUA) crystals. DTT_{COOH} reduced fouling by 75%, 86%, and 81% compared to bare crystal, UDT-, and MUA-coated surfaces, as far less material adsorbs onto the DTT_{COOH} surface.

As DTT's antifouling has been demonstrated in the literature, it was used to compare to DTT_{COOH}, which was derived from DTT. Following human serum incubation, the reso-

nant frequencies of DTT-coated crystals shifted by 100 ± 42 Hz while dissipation changed by $0.5 \pm 0.3 \times 10^{-5}$, indicating that minimal adsorption took place. The fouling trend of the bare and functionalized crystals is similar to their relative wettability based on their contact angles (Figure 8). However, DTT_{COOH} is less antifouling compared to DTT by about 21%. Although DTT_{COOH} is more hydrophilic than DTT, its carboxylic acid moiety is likely deprotonated in human serum, contributing to decreased antifouling capability by electrostatic interactions with serum components. As described in the introduction, previous work has shown that shifting from a hydroxyl to a carboxyl group increases fouling.

While a sole-DTT_{COOH} layer is less antifouling compared to DTT, its carboxyl group allows it to behave as a linker. Upon binding DTT_{COOH} to a desired receptor, the layer is expected to improve its antifouling character as the carboxyl group is modified. The data reported in Table 1 are shown in Figure 12.

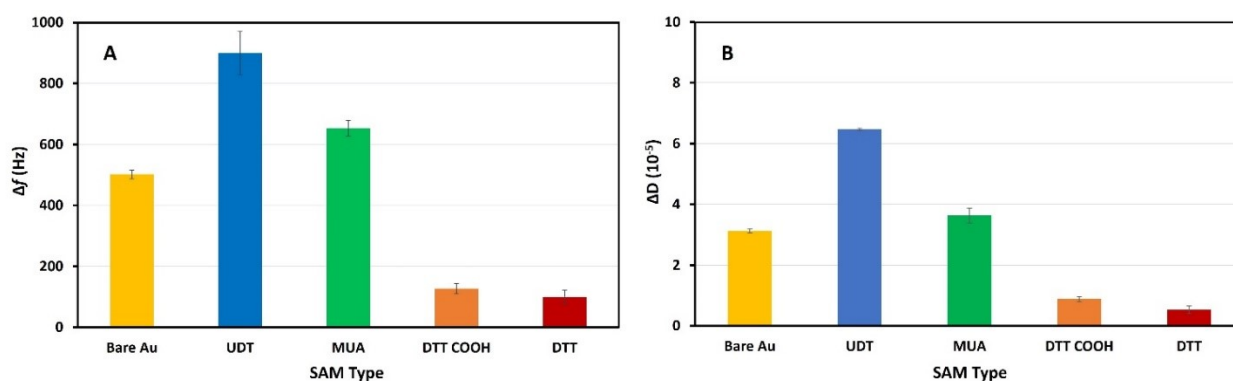


Figure 12. Frequency (A) and dissipation (B) shift of QCM crystals with different SAM coatings after exposure to undiluted human serum.

3.4. Antifouling Test of the Aptasensor

To examine DTT_{COOH}'s antifouling properties as a biosensor, it was linked to an aptamer for detecting penicillin via QCM-D (Figure 13). The aptasensor showed high selectivity to penicillin, as $10 \mu\text{M}$ of penicillin in undiluted human serum caused a high frequency shift of 90 Hz. Testing the aptasensor in undiluted serum without penicillin demonstrated significant antifouling as the frequency shifted by 25 Hz (Figure 13A). Compared to the DTT_{COOH}-only surface, which had a frequency shift of 127 Hz (Table 1), linking DTT_{COOH} with aptamer improved its antifouling by approximately 80%. Similarly, the aptasensor was 75% more antifouling relative to DTT surfaces. The fouling on the DTT_{COOH}-aptamer layer decreased by 95%, 96%, and 97% relative to bare crystal, MUA, and UDT surfaces.

Compared to non-antifouling surfaces (MUA, UDT, bare gold), the aptasensor had a low dissipation increase following exposure to undiluted serum (1.2×10^{-6}) as adsorption of serum species was minimal. However, after incubating the aptasensor in serum with $10 \mu\text{M}$ penicillin, the dissipation increased by 5.2×10^{-6} (Figure 13B). The much higher dissipation compared to serum without penicillin indicates the presence of adsorbed material on the surface, in which the most adsorbed components is penicillin binding to aptamer.

As discussed earlier, the improved antifouling of the aptasensor is likely due to modifying the carboxyl group to aptamer and ethanolamine, preventing the presence of negatively charged carboxylic acid groups in serum. Following elongation with aptamer and ethanolamine, the DTT_{COOH}-aptamer layer can maintain a hydration layer of interfacial water molecules via the polar hydroxyl groups and spacing between the propanoic acid chains, making NSA by serum components less favorable.

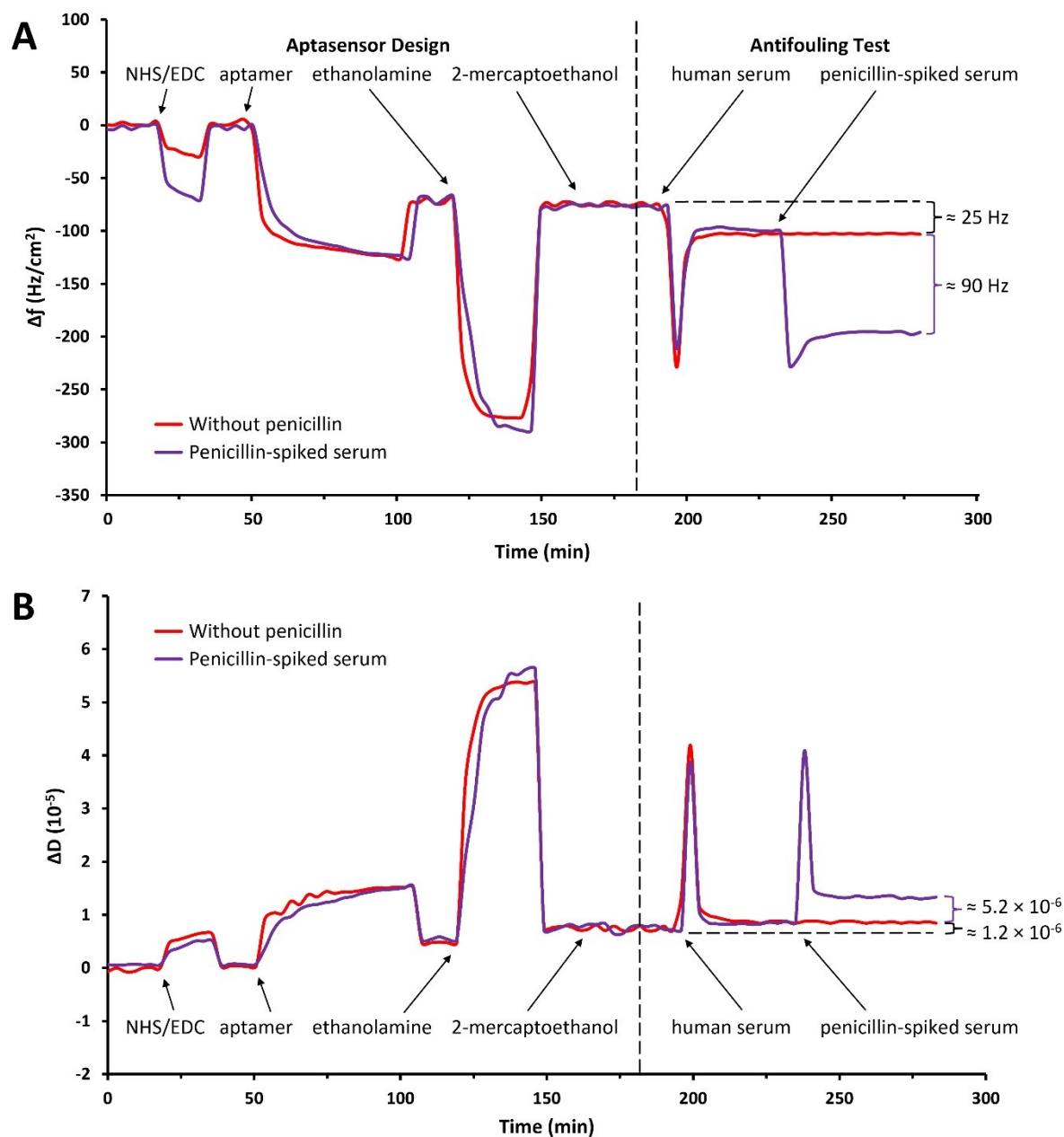


Figure 13. (A) Frequency and (B) dissipation variations when building the DTT_{COOH} aptasensor in-flow and testing its antifouling properties in undiluted human serum with and without 10 μ M penicillin.

4. Conclusions

In undiluted human serum, 3-dithiothreitol propanoic acid (DTT_{COOH}) significantly reduces non-specific adsorption. Its antifouling capability improved upon aptamer immobilization via DTT_{COOH}'s terminal carboxylic acid moiety. Our QCM-D results confirmed the antifouling properties of the aptasensor using DTT_{COOH} as a linker, as its frequency and dissipation shifts were minimal in undiluted human serum. The electrochemical stability of DTT_{COOH} on the gold electrode was confirmed with CV, which makes it a promising linker for developing electrochemical biosensors.

We plan to use DTT_{COOH} to develop biosensors with antifouling properties that can be used to detect various biomarkers in biofluidic samples such as plasma. Subsequent studies can investigate how to optimize the surface functionalization and improve DTT_{COOH} antifouling and linking properties. Currently, the focus of research is centered on character-

izing the surface modification of QCM-D crystals with DTT_{COOH} using X-ray photoelectron spectroscopy (XPS) and other techniques to complement the results. Plans are also in place to design alternative synthetic routes to prepare the DTT_{COOH} linker that would require fewer steps and less complicated workup processes.

Supplementary Materials: The following are available online at <https://www.mdpi.com/article/10.3390/chemosensors10100435/s1>, **SI:** NMR spectra of the compounds used for the development of antifouling linker. **SII:** Electrochemical properties of the gold electrodes following various modifications. Figure S1: ¹H NMR (400 MHz, DMSO) spectrum of oxidized-dithiothreitol (Ox-DTT): δ 5.19 (OH), 3.36 (H2, H3), 3.02 (H1, H4), 2.74 (H1, H4) ppm; Figure S2: ¹³C NMR (101 MHz, DMSO) spectrum of oxidized-dithiothreitol (Ox-DTT): δ 73.24 (C1, C4) and 40.20 (C2, C3) ppm; Figure S3: ¹³C NMR (126 MHz, CDCl₃, 0.05% w/v TMS) spectrum of tert-butyl 3-(DTT)propanoate (TBU-Ox-DTT): δ 170.67 (C1), 80.47 (C8), 75.74 (C4, C5), 64.42 (C3), 34.74 (C6, C7), 28.68 (C2), 27.05 (C9) ppm; Figure S4: ¹H NMR (500 MHz, CD₃CN) spectrum of 3-(DTT)propanoic acid (DTT_{COOH}): δ 5.93 (OH), 3.82 (H4, H5), 3.68 (H3), 3.00 (SH), 2.84 (H6, H7), 2.68 (H2) ppm; Figure S5: ¹³C NMR (126 MHz, CD₃CN) spectrum of 3-(DTT)propanoic acid (DTT_{COOH}): δ 163.74 (C1), 73.43 (C4, C5), 62.23 (C3), 40.89 (C2), 29.27 (C6, C7) ppm; Figure S6: Cyclic voltammogram (CV) of a gold electrode (blue line) after modification with DTT (green line), and further modification with aptamer (orange line). All experiments were carried out using a three-electrode set up with a gold electrode, a Pt wire, and Ag/AgCl electrode as working electrode, auxiliary electrode, and reference electrode, respectively, in 5 mM [Fe(CN)₆]^{3-/4-} as a redox probe containing 0.5 M KCl as a supporting electrolyte. CV experiments started at the open circuit potential (OCP) with positive initial scan polarity, and a sample interval of 2 mV; Figure S7: Influence of the scan rate, ν , on the CV electrochemical response of gold electrode after modification with DTT using 5 mM [Fe(CN)₆]^{3-/4-} as a redox probe containing 0.05 M KCl as a supporting electrolyte. All experiments were carried out using a three-electrode set up with a gold electrode, a Pt wire, and Ag/AgCl electrode as a working electrode, auxiliary electrode, and reference electrode, respectively. CV experiments started at the open circuit potential (OCP) with positive initial scan polarity, a sample interval of 2 mV, and a varying scan rate from 0.05 V/s to 1.0 V/s. (A) Cyclic voltammograms at different scan rates. (B) Graph of current vs square root of scan rate; Figure S8: Plot of the current vs square root of scan rate shows the influence of the scan rate on the CV electrochemical response of aptasensor using 5 mM [Fe(CN)₆]^{3-/4-} as a redox probe containing 0.5 M KCl as a supporting electrolyte. All experiments were carried out using a three-electrode set up with a gold electrode, a Pt wire, and Ag/AgCl electrode as working electrode, auxiliary electrode, and reference electrode, respectively. CV experiments started at the open circuit potential (OCP) with positive initial scan polarity, a sample interval of 2 mV, and a varying scan rate from 0.05 V/s to 1.0 V/s.

Author Contributions: Conceptualization, S.S., T.H. and M.T.; formal analysis, S.S., K.D., S.A. and E.C.; investigation, S.S., K.D., S.A. and E.C.; methodology, S.S., T.H. and M.T.; validation, S.S.; funding acquisition, T.H. and M.T.; project administration, T.H. and M.T.; supervision, T.H. and M.T.; writing—original draft, S.S., K.D., S.A. and E.C.; writing—review & editing, S.S., T.H. and M.T. All authors have read and agreed to the published version of the manuscript.

Funding: This work was funded under European Union's Horizon 2020 research and innovation program through the Marie Skłodowska-Curie grant agreement No. 101007299 (T.H. and M.T.), The Science Agency VEGA, project No. 1/0419/20 (T.H.), and by the Natural Sciences Engineering Research Council of Canada (M.T., NSERC 9522).

Institutional Review Board Statement: Not applicable.

Informed Consent Statement: Not applicable.

Data Availability Statement: Not applicable.

Acknowledgments: The authors are grateful to Brian De La Franier of the University of Toronto, Canada, for much helpful discussion, and to Eric S. Muckley of Citrine Informatics (San Francisco, USA) for providing software support.

Conflicts of Interest: The authors declare no conflict of interest.

References

1. Spagnolo, S.; De La Franier, B.; Hianik, T.; Thompson, M. Surface probe linker with tandem anti-fouling properties for application in biosensor technology. *Biosensors* **2020**, *10*, 20. [[CrossRef](#)] [[PubMed](#)]
2. Campuzano, S.; Kuralay, F.; Lobo-Castañón, M.J.; Bartošik, M.; Vyavahare, K.; Paleček, E.; Haake, D.A.; Wang, J. Ternary monolayers as DNA recognition interfaces for direct and sensitive electrochemical detection in untreated clinical samples. *Biosens. Bioelectron.* **2011**, *26*, 3577–3583. [[CrossRef](#)] [[PubMed](#)]
3. Chen, S.; Li, L.; Zhao, C.; Zheng, J. Surface hydration: Principles and applications toward low-fouling/nonfouling biomaterials. *Polymer* **2010**, *51*, 5283–5293. [[CrossRef](#)]
4. Del Grosso, C.A.; Leng, C.; Zhang, K.; Hung, H.-C.; Jiang, S.; Chen, Z.; Wilker, J.J. Surface hydration for antifouling and bio-adhesion. *Chem. Sci.* **2020**, *11*, 10367–10377. [[CrossRef](#)]
5. Pawlowska, N.M.; Fritzsche, H.; Blaszykowski, C.; Sheikh, S.; Vezvaie, M.; Thompson, M. Probing the hydration of ultrathin antifouling organosilane adlayers using neutron reflectometry. *Langmuir* **2014**, *30*, 1199–1203. [[CrossRef](#)]
6. Sheikh, S.; Blaszykowski, C.; Nolan, R.; Thompson, D.; Thompson, M. On the hydration of subnanometric antifouling organosilane adlayers: A molecular dynamics simulation. *J. Colloid Interface Sci.* **2015**, *437*, 197–204. [[CrossRef](#)]
7. Avci, C.; Sheikh, S.; Blaszykowski, C.; Thompson, M. Critical role of surface hydration on the dynamics of serum adsorption studied with monoethylene glycol adlayers on gold. *Chem. Commun.* **2012**, *49*, 466–468. [[CrossRef](#)]
8. Spagnolo, S.; De La Franier, B.; Davoudian, K.; Hianik, T.; Thompson, M. Detection of *E. coli* bacteria in milk by an acoustic wave aptasensor with an anti-fouling coating. *Sensors* **2022**, *22*, 1853. [[CrossRef](#)]
9. Chávez, M.; Sánchez-Obrero, G.; Madueño, R.; Sevilla, J.M.; Blázquez, M.; Pineda, T. Characterization of a self-assembled monolayer of O-(2-Mercaptoethyl)-O'-Methyl-Hexa(ethylene Glycol) (EG7-SAM) on gold electrodes. *J. Electroanal. Chem.* **2021**, *880*, 114892. [[CrossRef](#)]
10. Raymundo-Pereira, P.A.; de Oliveira Pedro, R.; Carr, O.; Melendez, M.E.; Gobbi, A.L.; de Oliveira Piazzetta, M.H.; Carvalho, A.L.; Reis, R.M.; Miranda, P.B.; Oliveira, O.N., Jr. Influence of the molecular orientation and ionization of self-assembled monolayers in biosensors: Application to genosensors of prostate cancer antigen 3. *J. Phys. Chem. C* **2021**, *125*, 498–506. [[CrossRef](#)]
11. Hianik, T. Advances in electrochemical and acoustic aptamer-based biosensors and immunosensors in diagnostics of leukemia. *Biosensors* **2021**, *11*, 177. [[CrossRef](#)]
12. Bertok, T.; Dosekova, E.; Belicky, S.; Holazova, A.; Lorencova, L.; Mislovicova, D.; Paprckova, D.; Vikartovska, A.; Plicka, R.; Krejci, J.; et al. Mixed zwitterion-based self-assembled monolayer interface for impedimetric glycomic analyses of human IgG samples in an array format. *Langmuir* **2016**, *32*, 7070–7078. [[CrossRef](#)]
13. Wu, J.; Campuzano, S.; Halford, C.; Haake, D.A.; Wang, J. Ternary surface monolayers for ultrasensitive (zeptomole) amperometric detection of nucleic acid hybridization without signal amplification. *Anal. Chem.* **2010**, *82*, 8830–8837. [[CrossRef](#)]
14. Spagnolo, S.; Muckley, E.S.; Ivanov, I.N.; Hianik, T. Analysis of trypsin activity at β -casein layers formed on hydrophobic surfaces using a multiharmonic acoustic method. *Analyst* **2022**, *147*, 461–470. [[CrossRef](#)]
15. Tonda-Turo, C.; Carmagnola, I.; Ciardelli, G. Quartz crystal microbalance with dissipation monitoring: A powerful method to predict the in vivo behavior of bioengineered surfaces. *Front. Bioeng. Biotechnol.* **2018**, *6*, 158. [[CrossRef](#)]
16. Spagnolo, S.; Muckley, E.S.; Ivanov, I.N.; Hianik, T. Application of multiharmonic QCM-D for detection of plasmin at hydrophobic surfaces modified by β -casein. *Chemosensors* **2022**, *10*, 143. [[CrossRef](#)]
17. Tatarko, M.; Spagnolo, S.; Oravczová, V.; Süle, J.; Hun, M.; Hucker, A.; Hianik, T. Changes of viscoelastic properties of aptamer-based sensing layers following interaction with *Listeria innocua*. *Sensors* **2021**, *21*, 5585. [[CrossRef](#)]
18. Muckley, E.S.; Collins, L.; Srijanto, B.R.; Ivanov, I.N. Machine learning-enabled correlation and modeling of multimodal response of thin film to environment on macro and nanoscale using Lab-on-a-Crystal. *Adv. Funct. Mater.* **2020**, *30*, 1908010. [[CrossRef](#)]
19. Yoon, S.M.; Cho, N.J.; Kanazawa, K. Analyzing spur-distorted impedance spectra for the QCM. *J. Sens.* **2009**, *2009*, 259746. [[CrossRef](#)]
20. Mann, M.A.; Bottomley, L.A. Cyclic square wave voltammetry of surface-confined quasireversible electron transfer reactions. *Langmuir* **2015**, *31*, 9511–9520. [[CrossRef](#)]
21. Zina, F.; Nooredeen, N.M.; Azzouzi, S.; Ali, M.B.; Abbas, M.N.; Errachid, A. Novel sensitive impedimetric microsensor for phosphate detection based on a novel copper phthalocyanine derivative. *Anal. Lett.* **2018**, *51*, 371–386. [[CrossRef](#)]
22. Mattiuzzi, A.; Troian-Gautier, L.; Mertens, J.; Reniers, F.; Bergamini, J.-F.; Lenne, Q.; Lagrost, C.; Jabin, I. Robust hydrophobic gold, glass and polypropylene surfaces obtained through a nanometric covalently bound organic layer. *RSC Adv.* **2020**, *10*, 13553–13561. [[CrossRef](#)] [[PubMed](#)]
23. Ahmad, A.; Moore, E. Electrochemical immunosensor modified with self-assembled monolayer of 11-mercaptoundecanoic acid on gold electrodes for detection of benzo[a]pyrene in water. *Analyst* **2012**, *137*, 5839–5844. [[CrossRef](#)] [[PubMed](#)]
24. Kochana, J.; Starzec, K.; Wieczorek, M.; Knihnicki, P.; Góra, M.; Rokicińska, A.; Kościelniak, P.; Kuśtrowski, P. Study on self-assembled monolayer of functionalized thiol on gold electrode forming capacitive sensor for chromium(VI) determination. *J. Solid State Electrochem.* **2019**, *23*, 1463–1472. [[CrossRef](#)]
25. Guo, Y.; Chen, M.; He, H. Alkyl chain dependent alkanethiol self-assembled adsorption dynamics. *Surf. Rev. Lett.* **2015**, *22*, 1550004. [[CrossRef](#)]
26. Thébault, P.; Ammoun, M.; Boudjema, R.; Ouvrard, A.; Steenkeste, K.; Bourguignon, B.; Fontaine-Aupart, M.-P. Surface functionalization strategy to enhance the antibacterial effect of nisin Z peptide. *Surf. Interfaces* **2022**, *30*, 101822. [[CrossRef](#)]

27. MacDairmid, A.R.; Gallagher, M.C.; Banks, J.T. Structure of dithiothreitol monolayers on Au(111). *J. Phys. Chem. B* **2003**, *107*, 9789–9792. [[CrossRef](#)]
28. Nuzzo, R.G.; Allara, D.L. Adsorption of bifunctional organic disulfides on gold surfaces. *J. Am. Chem. Soc.* **1983**, *105*, 4481–4483. [[CrossRef](#)]
29. Alawad, A.; Istamboulié, G.; Calas-Blanchard, C.; Noguier, T. A reagentless aptasensor based on intrinsic aptamer redox activity for the detection of tetracycline in water. *Sens. Actuators B Chem.* **2019**, *288*, 141–146. [[CrossRef](#)]
30. Paleček, E.; Bartošik, M. Electrochemistry of nucleic acids. *Chem. Rev.* **2012**, *112*, 3427–3481. [[CrossRef](#)]
31. Wang, H.-S.; Ju, H.-X.; Chen, H.-Y. Simultaneous determination of guanine and adenine in DNA using an electrochemically pretreated glassy carbon electrode. *Anal. Chim. Acta* **2002**, *461*, 243–250. [[CrossRef](#)]
32. Kerman, K.; Morita, Y.; Takamura, Y.; Ozsoz, M.; Tamiya, E. DNA-directed attachment of carbon nanotubes for enhanced label-free electrochemical detection of DNA hybridization. *Electroanalysis* **2004**, *16*, 1667–1672. [[CrossRef](#)]
33. Urmann, K.; Modrejewski, J.; Scheper, T.; Walter, J.-G. Aptamer-modified nanomaterials: Principles and applications. *BioNanoMaterials* **2017**, *18*, 20160012. [[CrossRef](#)]
34. Tan, S.Y.; Acquah, C.; Tan, S.Y.; Ongkudon, C.M.; Danquah, M.K. Characterisation of charge distribution and stability of aptamer-thrombin binding interaction. *Process. Biochem.* **2017**, *60*, 42–51. [[CrossRef](#)]